

Near Large Far Small: Relative Distance Based Partition Learning for UAV-view Geo-Localization

Quan Chen, Tingyu Wang, Rongfeng Lu, Bolun Zheng, Zhedong Zheng and Chenggang Yan

Abstract—UAV-view Geo-Localization (UVGL) presents substantial challenges, primarily due to appearance differences between drone-view and satellite-view. Existing methods develop partition learning strategies aimed at mining more comprehensive information by constructing diverse part-level feature representations, which rely on consistent cross-view scales. However, variations of UAV flight state leads to the scale mismatch of cross-views, resulting in serious performance degradation of partition-based methods. To overcome this issue, we propose a partition learning framework based on relative distance, which alleviates the dependence on scale consistency while mining fine-grained features. Specifically, we propose a distance guided dynamic partition strategy (DGDPL), consisting of a square partition strategy and a dynamic-guided adjustment strategy. The former is utilized to extract fine-grained features and global features in a simple manner. The latter calculates the relative distance ratio between drone- and satellite-view to adjust the partition size, thereby aligning the semantic information between partition pairs. Furthermore, we propose a saliency-guided refinement strategy to refine part-level features, so as to further improve the retrieval accuracy. Extensive experiments show that our approach achieves superior geo-localization accuracy across various scale-inconsistent scenarios, and exhibits remarkable robustness against scale variations. The code will be released.

Index Terms—image retrieval, geo-localization, dynamic partition, relative distance ratio, scale variations

I. INTRODUCTION

UNMANNED Aerial Vehicles (UAVs) have gained popularity due to their ability to efficiently capture data with few occlusions and rich content. Differ from ground-views, UAVs can easily acquire multi-resolution images by changing the flight altitude and camera parameters. Benefiting from these advantages, UAVs play an irreplaceable role in various fields, including agricultural operations [1], automatic driving [2] and aerial photography [3]. Regardless of the applications, precise positioning and navigation of UAVs are indispensable, which mainly rely on a global navigation satellite system (GNSS) and high-quality communication environment [4]. In scenarios with weak or failed signals, GNSS will incorrectly determine the geographic localization of UAVs.

Quan Chen, Rongfeng Lu, Bolun Zheng and Chenggang Yan are with the School of Automation, Hangzhou Dianzi University, Hangzhou 310018, China (e-mail: chenquan@hdu.edu.cn; blzheng@hdu.edu.cn; cgyan@hdu.edu.cn).

Tingyu Wang is with the School of Communication Engineering, Hangzhou Dianzi University, Hangzhou 310018, China, and also with the Lishui Institute of Hangzhou Dianzi University, Lishui 323000, China (e-mail: wongtyu@hdu.edu.cn).

Zhedong Zheng is with the Faculty of Science and Technology, and Institute of Collaborative Innovation, University of Macau, Macau, China (e-mail: zhedongzheng@um.edu.mo).

Tingyu Wang and Bolun Zheng are the Corresponding Authors.

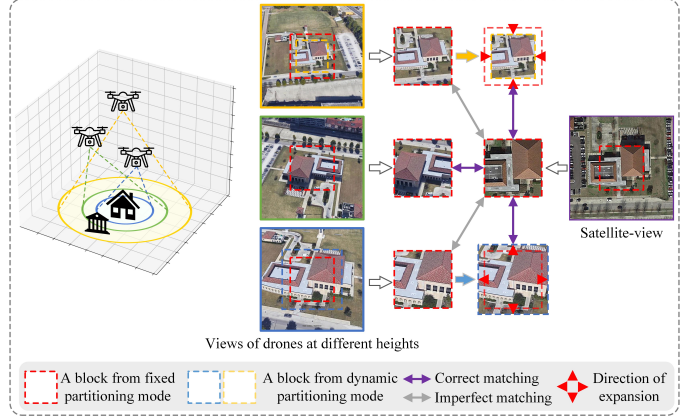


Fig. 1. The simplified diagram of our research motivation. Given drone-view images captured from different altitudes (high-yellow box, middle-green box, low-blue box) and the matched satellite-view image, part-level image representations are constructed using a fixed partition strategy and our dynamic partition strategy, respectively. As can be observed, the extended/indented partition pairs have more consistent semantic content.

Therefore, vision-based UAV-view geo-localization (UVGL) develops a meaningful hot research, aiming to release the dependence on GNSS. As the key of this task, cross-view matching algorithms calculate the similarity between drone- and satellite-view images to achieve image matching. However, due to the appearance difference such as scale and color between drone-views and satellite-views, traditional image matching algorithms [5]–[7] are imprecise.

With the rapid development of deep learning, current methods [8]–[14] utilize pre-trained backbone networks to extract high-level semantic representations and perform image matching based on feature distances, achieving superior accuracy than non-learning-based algorithms. To obtain robust discriminative representations, plentiful partition learning strategies have been proposed, which construct fine-grained features by segmenting high-level features to fully exploit contextual information. Depending on the pattern of feature segmentation, partition learning can be divided into two categories: **soft-partition** learning [15]–[19] and **hard-partition** learning [20]–[25]. The former classifies features based on feature values to distinguish the categories of semantic information, so the shape of partitions is uncontrollable. FSRA [15], as a representative of soft-partition learning, confirms that fine-grained features have a consistent distribution with image content and can boost model performance. In contrast, inspired by the distribution similarity between drone- and satellite-views, hard-partition strategies set templates of fixed size and shape to

segment high-level features. As the pioneering hard-partition algorithm, LPN [20] designs non-overlapping square-ring templates to build fine-grained features. Subsequently, several studies [26]–[28] further optimize the shape and number of templates to facilitate discriminative representation. Benefiting from the explicit utilization of contextual information, hard-partition strategies reveal superior accuracy and compatibility than soft-partition strategies under same settings. Nevertheless, hard-partition strategies are more sensitive to spatial changes of input images. During the data collection process, changes of UAV flight state will cause misalignment of cross-view images, including position offset and scale change. The fixed segmentation templates constrain misaligned semantic information to same parts, thus interfering with feature matching.

However, there is currently no method to alleviate the dependence of hard-partition learning on cross-view scale consistency. As shown in Fig. 1, we depict the limitation of hard-partition strategies in dealing with scale-misaligned image pairs. Taking LPN [20] as an example, the partition pairs contain similar semantic information in the case of similar cross-view scales (see drone-view with green box). When UAV altitude changes, partition pairs of fixed shape contain misaligned semantic information, defined as imperfect matching (see drone-view with yellow or blue box). Following the imaging law of “near large far small” in photography, we argue that adjusting the partition size based on the shooting distance of the UAV can ensure the content consistency of partition pairs, thus boosting the matching of cross-view partition pairs. Concretely, for high-altitude (*i.e.*, long distance) UAV-view, indent templates can reduce redundancy in the part-level representations, while expanded templates contributes to the content supplement of partitions for low-altitude (*i.e.*, short distance) UAV-view. Imitating the process mentioned above, we propose a distance guided dynamic partition learning framework named DGDPL, to enhance the content consistency of partition pairs when the shooting distance of UAV changed. Specifically, we design a square partition strategy (SPS) as shown in Case(II) of Fig. 2, which has two typical advantages: 1) multiple partitions constructed by SPS emphasize both fine-grained and global features, thereby exhibiting robustness against scale variations; 2) solid partitions are readily generated and have strong compatibility with subsequent algorithms. To promote the content consistency of partition pairs, we further propose a distance-guided adjustment strategy (DGAS). We construct a scale factor β to represent the relative distance of drone- and satellite-view, and inject it into SPS to dynamically adjust the partition size of drone-views. As shown in Case(I) and Case(III) of Fig. 2, our DGAS controls variations of partitions, both in direction and degree. Furthermore, we design a saliency-guided refinement strategy (SGRS) to identify targets and environments based on feature activation degrees. The SGRS maintains robustness to scale changes while improving model matching accuracy. Extensive experiments on University-1652 show that our DGDPL framework exhibits excellent robustness to cross-view scale changes, and achieves remarkable performance in scenarios with inconsistent cross-view scales. For instance, the average R@1 of our DGDPL on multiple scale scenarios is nearly

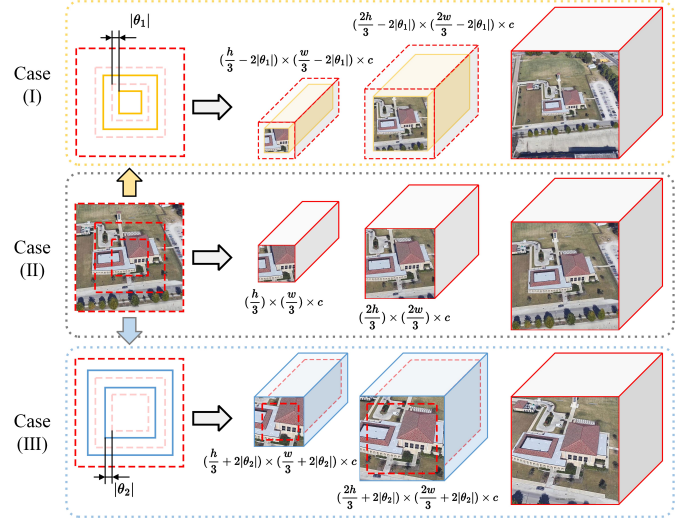


Fig. 2. Distance guided dynamic partition learning strategy ($N = 3$ for illustration). Case(II): the default square partition process, *i.e.*, the partition size of satellite- and drone-view is same. Case(I): the partitions are indented based on scale factor $\theta_1 (> 0)$ to fit the drone-view with long distance. Case(III): the partitions are expanded based on scale factor $\theta_2 (< 0)$ to fit the drone-view with short distance. Note that as a global feature, the size of the last partition is constant.

30.70% and 16.64% higher than that of baseline and LPN, respectively.

Our main contributions are as follows:

- We propose DGDPL, including a square partition strategy and a distance-guided adjustment strategy, to achieve accurate UAV-view geo-localization against scale variations of drone-views.
- We formulate a saliency-guided refinement strategy to refine part-level features, thus improving retrieval accuracy while maintaining robustness to scale changes.
- Extensive experiments show that, in comparison to both hard-partition and soft-partition strategies, our method achieves splendid retrieval performance in scenes with inconsistent cross-view scales.

The rest of the paper is organized as follows: Section II presents related work, focusing on cross-view geo-localization and part-based representation learning. In Section III, we detail our proposed method, including the method overview and each component. Section IV presents our experimental results, and Section V provides concluding remarks.

II. RELATED WORK

We briefly review related work, including cross-view geo-localization and part-based representation learning.

A. Cross-view Geo-localization

Cross-view Geo-localization aims to recognize the geographic location of an input image based on satellite database, which mainly emphasizes two distinct matching tasks, *i.e.*, the matching of ground and satellite views, as well as the matching of drone and satellite views. Traditional methods [5]–[7] rely on hand-crafted feature, yet their precision is seriously constrained by appearance differences of cross-view images.

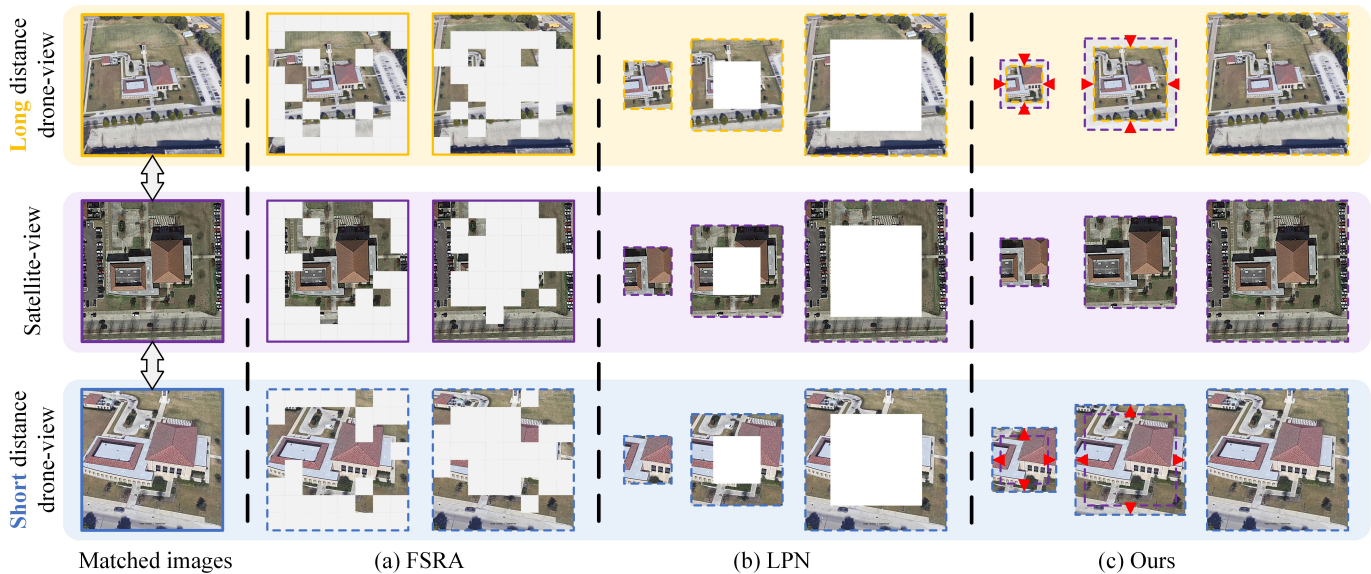


Fig. 3. The comparison of our method with typical partition strategies, including soft-partition strategy (a) FSRA [15] and hard-partition strategy (b) LPN [20]. The first and third rows are drone-view images with long and short distance, while the second row is the matched satellite image with a single scale. For different partition strategies, matched part-level image representations are placed in the same column.

Benefiting from the powerful representation ability of neural networks, prevalent methods employ pre-trained backbone networks to extract deep features, thereby enabling cross-view image matching within a high-dimensional space. Numerous works [29]–[36] have driven the development of the matching of ground and satellite views in terms of data and algorithms. For instance, CVUSA [31], CVACT [32] and Vigor [35] are extensively utilized as benchmark datasets to evaluate algorithm performance. Deuser *et al.* [33] designed GPS-sampling and dynamic similarity sampling to select hard negatives, leading to superior results on several datasets. To release the cost of collecting precise pairwise data, Li *et al.* [37] proposed a unsupervised framework to utilize unlabeled data in ground-view geo-localization. In addition, image synthesis methods [38]–[40] minimizing appearance differences of cross-views, can significantly improve the matching accuracy.

With the growing popularity of UAV devices, several datasets [41]–[43] introduced drone-view images to support for the UVGL task. Zheng *et al.* [8] collected the University-1652 dataset, which contains pairs of ground-views, drone-views and satellite-views. Notably, Zheng [8] introduced variations in both the shooting angle and shooting distance of drone-views, thus enhancing the diversity of University-1652. To investigate effects of drone-views at various heights on geo-localization, Zhu *et al.* [41] developed SUES-200 comprising UAV images acquired at four altitudes. DenseUAV [42], as the pioneering low-altitude urban scene dataset, was tailored for the UAV self-positioning task (*i.e.*, geo-localization within continuous local areas). Focusing on inaccurate alignment between query images and corresponding labels, GTA-UVA [43] dataset introduced semi-positive samples to simulate imperfect matching. Despite viewpoint changes compared to ground-view geo-localization, mainstream solutions [8]–[11], [44]–[49] converged upon a similar principle: mapping multi-view

images into a shared high-dimensional space, subsequently facilitating image matching through similarity calculation. Several studies [15], [22], [50] proved that stronger backbone networks can significantly improve the accuracy of UVGL. Sun *et al.* [47] designed a specific feature extractor named F3-Net to capture both local and global information. RK-Net [10] inserted unit subtraction attention modules inside the backbone to detect representative keypoints, yielding robust features against viewpoints. Considering the color discrepancy between drone-views and satellite-views, recent methods [51]–[53] adjusted the color distribution of drone-views to reduce domain gaps. Some efforts [16], [46], [54] improved the optimization function in the training phase to facilitate domain alignment of cross-view images. To obtain robust semantic representations, plentiful partition learning strategies are also introduced, which will be detailed in next subsection. In this paper, we propose a UAV-view geo-localization algorithm applicable to scenes with inconsistent cross-view scales. To meet the requirements of scale inconsistency and scene diversity, we conduct experiments on University-1652 [8].

B. Part-based Representation Learning

Fine-grained features guide models to capture more comprehensive information, which has been proven effective in many fields, such as image restoration [55]–[57] and segmentation [58]–[60]. Inspired by classical part-based descriptors [61]–[63], numerous works in person re-identification [64]–[70] developed local feature representation by introducing human body structure information. For instance, Spindle-Net [64] leveraged body joints to capture consistent body features from different images, thus enabling the alignment of macro- and micro-body features across images. To eliminate the dependence on skeleton points,

researchers further proposed coarse partition strategies rooted in the vertical distribution of the human body [68]–[70].

Previous research has laid the foundation for partition learning in UVGL, which can be divided into two categories based on the pattern of feature segmentation: **soft-partition** learning [15]–[18] and **hard-partition** learning [20]–[25]. Soft-partition strategies, represented by FSRA [15], leverage feature values to distinguish categories of semantic information. Subsequently, TransFG [16] adopts the second-order gradient of features as the partition index, yielding a decent performance boost. FSRA and TransFG divided features equally based on the setting that each part has equal area, resulting in misalignment of cross-view partition pairs in both large-scale and small-scale scenes. To address this issue, GeoFormer [17] utilized a k-modes clustering algorithm to divide features adaptively. However, the above soft-partition strategies rely on the transformer framework [71]. Drawing upon the similarity between drone- and satellite-views, some methods employ fixed templates to generate fine-grained features, which are defined as hard-partition strategies. LPN [20] designed non-overlapping square-ring templates to segment features, thus mining contextual information. Based on LPN, several studies [24]–[28] optimized the shape and number of templates to further facilitate discriminative representation. Aiming at the problem of position offset, SDPL [50] proposed a shifting-fusion strategy, which adjusts the segmentation center to align partitions with non-centered targets. The hard partition strategies exhibit commendable accuracy and compatibility, while being sensitive to cross-view scale variation.

To visually reveal the dependence of partition learning on cross-view scales, we illustrate two representative methods (FSRA [15] and LPN [20]) for dealing with long distance scenes and short distance scenes, as shown in Fig. 3. Limited to the setting where the partition area is the same, FSRA divided features of different categories into the same partition, resulting in feature misalignment. LPN employed fixed templates to generate fine-grained features. Notably, in scenarios where cross-view scales are inconsistent, partition pairs contain misaligned semantic content. In this paper, we study a part-based representation learning for UVGL. In comparison with soft-partition strategies, our method achieves superior performance and compatibility, whereas, in contrast to hard-partition strategies, it exhibits enhanced robustness against scale variations.

III. METHODS

As depicted in Fig. 4, our DGDPL framework consists of three stages: feature extraction, distance guided dynamic partition learning and classification supervision. In the feature extraction stage, a backbone network maps drone- and satellite-view images to high-level feature maps. Then, we introduce distance guided dynamic partition learning to generate fine-grained features with consistent content. We also propose a saliency-guided refinement strategy to identify differences within part-level features. Finally, we adopt a classifier to predict the category of features obtained from different views, followed by using cross-entropy loss to optimize the model.

Task definition. The geo-localization dataset contains images pairs captured from different platforms, defined as $\{x_D, x_S\}$, where subscripts D and S indicate drone- and satellite-view, respectively. We denote the label as $y \in [1, C]$, where C indicates the number of categories. For instance, the label of University-1652 [8] dataset is $y \in [1, 701]$. For UAV-view geo-localization, we intend to learn a mapping function that projects images from various platforms to one shared semantic space. Image pairs with the same geo-tag have a consistent spatial distribution (*i.e.*, close to each other), otherwise, the image pairs are far apart from each other.

A. Feature Extraction

Both drone-view and satellite-view images fall within the category of aerial-view imagery, exhibiting comparable feature domains. Consequently, We employ one feature extractor to process cross-view images. As mentioned before, our DGDPL belongs to hard-partition learning and is compatible with various backbone networks, such as ResNet [72] and ViT [71]. Following previous works [20], [50], we adopt ResNet-50 for illustration. Given an image $x_i \in \mathbb{R}^{3 \times 512 \times 512}$, after the backbone network and an upsampling layer we can acquire the corresponding high-level feature map $f_i \in \mathbb{R}^{2048 \times 32\lambda \times 32\lambda}$. The process can be formulated as:

$$f_i = \mathcal{U}_\lambda(\mathcal{F}_{backbone}(x_i)), i \in \{D, S\} \quad (1)$$

where $\mathcal{F}_{backbone}$ stands for the process of feature extraction, and \mathcal{U}_λ stands for the upsampling process with scale factor λ . We emphasize that the degree of variation in partition size can be refined by upsampling feature map f_i .

B. Distance Guided Dynamic Partition Learning

To capture aligned contextual information even in scale-inconsistent scenes, we propose a distance guided dynamic partition learning, consisting of a square partition strategy, a distance-guided adjustment strategy, and a saliency-guided refinement strategy.

Square partition strategy (SPS). We propose a simple yet effective partition strategy to generate fine-grained features. As shown in Case(II) of Fig. 2, our square partition strategy splits the input feature into N_{SPS} parts following square templates. Concretely, after SPS processing, the high-level feature map $f_i \in \mathbb{R}^{2048 \times 32\lambda \times 32\lambda}$ is segmented into N_{SPS} part-level feature $f_i^{n_{SPS}} \in \mathbb{R}^{2048 \times \frac{32\lambda n_{SPS}}{N_{SPS}} \times \frac{32\lambda n_{SPS}}{N_{SPS}}}$ ($n_{SPS} \in [1, N_{SPS}]$), where n_{SPS} denotes the n -th part. The overall SPS processing can be formulated as:

$$\Omega(f_i^{n_{SPS}}) = \{f_i^{n_{SPS}} | \mathcal{F}_{SPS}(f_i; N_{SPS})\} \quad (2)$$

where $\mathcal{F}_{SPS}(\cdot)$ stands for the process of SPS, and $\Omega(f_i^{n_{SPS}})$ denotes the set of all fine-grained features.

Despite the similarities with LPN, by comparing Fig. 3 (b) and (c) we state that SPS has two distinct advantages: 1) SPS mines local features while maintaining global information, enhancing robustness against scale changes; 2) the solid partition is readily obtainable and its size can be easily adjusted.

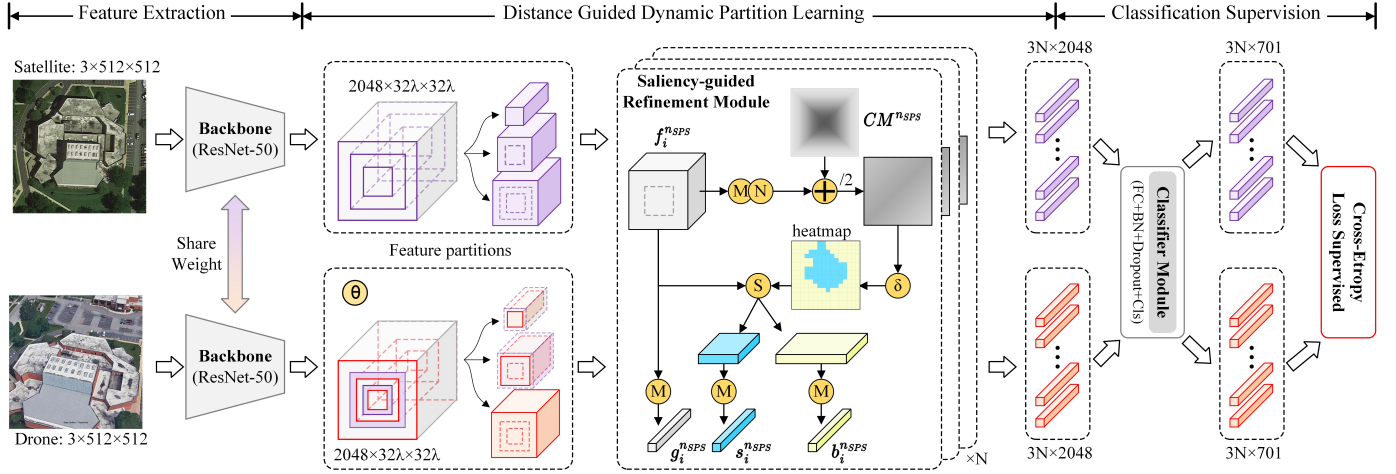


Fig. 4. Overview of DGDPL framework, including three phase: feature extraction, altitude guided dynamic partition learning and classification supervision. In the testing phase, part-level image representation is extracted before classification layer in classifier module, and measures similarity by Euclidean distance.

Distance-guided adjustment strategy (DGAS). Existing hard-partition methods utilize uniform templates for processing multi-view images. However, in scenarios where drone-view scale undergo significant variations, these methods exhibit notable performance degradation. The primary reason is the misalignment of semantic content within partition pairs. To solve this limitation, we propose an innovative distance-guided adjustment strategy, *i.e.*, dynamically adjusting partition size in response to drone-view scale changes, thus boosting content consistency between partition pairs.

Specifically, both the pose of UAVs and the resolution of satellite maps belong to additional attributes which can be obtained in the GPS-denied environment. Based on these attributes, the distance between drone/satellite-views and the ground can be estimated, linearly related to the image scale. In this paper, we assume that the distance between drone/satellite-views to the ground is known. Then, we introduce a scale factor β to quantify the relative distance between cross-view images:

$$\beta = \frac{H_D - H_S}{H_S} \quad (3)$$

where H_D and H_S denote the distance from drone-view and satellite-view to the ground, respectively. Note that the satellite-view distance H_S is constant, which is the regular setting for UVGL.

Since modifying partitions in high-dimensional space instead of RGB domain, we further construct the adjustment factor θ based on β :

$$\theta = \text{int}(\beta \cdot \lambda \cdot \alpha) \quad (4)$$

where $\text{int}(\cdot)$ stands for the round operation, λ denotes the upsampling factor mentioned in Eq.(1), and α denotes the hyper-parameter utilized to regulate the degree of partition change. The sign of θ is determined by β , where ($\theta > 0$) denotes indenting partitions, whereas ($\theta < 0$) denotes expanding partitions.

Then, we inject θ into SPS to adjust partitions of drone-views, which can be formulated as:

$$\Omega(f_D^{n_{SPS}}) = \{f_D^{n_{SPS}} | \mathcal{F}_{SPS}^D(f_D; N_{SPS}; \theta)\} \quad (5)$$

where $\mathcal{F}_{SPS}^D(\cdot)$ denotes the process of SPS specific for drone-views. For ease of understanding, we depict the \mathcal{F}_{SPS}^D process in two cases (*i.e.*, $\theta > 0$ and $\theta < 0$), as shown in Fig. 2 (Case I and III). We employ θ to adjust the size of partitions, and the shape of each partition pair is expressed as follows:

$$\begin{cases} f_D^{n_{SPS}} \in \mathbb{R}^{2048 \times (\frac{32\lambda n_{SPS}}{N_{SPS}} - 2\theta) \times (\frac{32\lambda n_{SPS}}{N_{SPS}} - 2\theta)} \\ f_S^{n_{SPS}} \in \mathbb{R}^{2048 \times (\frac{32\lambda n_{SPS}}{N_{SPS}}) \times (\frac{32\lambda n_{SPS}}{N_{SPS}})} \end{cases} \quad (6)$$

Note that the global feature $f_D^{n_{SPS}}$ is invariant.

In practice, the size of partitions must be positive. In other words, when $\theta > 0$, θ must adhere to the following constraint:

$$\max(|\theta|) \leq \frac{32\lambda}{2N_{SPS}} - 1 \quad (7)$$

Based on Eq. (3), (4) and (7), we can derive the range of α :

$$0 \leq \alpha \leq \frac{16\lambda - N_{SPS}}{N_{SPS}} \cdot \frac{1}{\lambda} \cdot \frac{H_S}{\max(H_D) - H_S} \quad (8)$$

where $\max(H_D)$ denotes the maximum distance of drone-views. When $\alpha < 0$, the extreme case is that all partitions expand equal to the global feature, thereby necessitating no constraint on the value range of α . Hence it suffices to constrain α based on Eq. (8). Note that we omit the effect of lens focal length on the drone-view scale and default to a uniform lens setting for drone-view images. Therefore, α can be selected experimentally.

Saliency-guided refinement strategy (SGRS). Each solid partition inherently contains both target and environment information. To further refine part-level features, we design a saliency-guided refinement strategy. The overall process are depicted in Fig. 4, and can be expressed as:

$$(g_i^{n_{SPS}}, s_i^{n_{SPS}}, b_i^{n_{SPS}}) = \mathcal{F}_{SGRS}(f_i^{n_{SPS}}) \quad (9)$$

where $\mathcal{F}_{SGRS}(\cdot)$ denotes the process of SGRS, and $g_i^{n_{SPS}}$, $s_i^{n_{SPS}}$, $b_i^{n_{SPS}}$ are denote the output global feature, salient feature and background feature, respectively.

Specifically, assuming the input partition feature is $f_i^{n_{SPS}} \in \mathbb{R}^{2048 \times h \times w}$, we first generate the heatmap $heat_i^{n_{SPS}} \in \mathbb{R}^{1 \times h \times w}$ to reflect importance regions of the input. Considering that targets are usually centered, we introduce an auxiliary coordinate map (CM) to direct the heatmap's focus towards the central region. The CM indicates inverse pixel-to-center distance, ranging from 1 (center) to 0 (farthest). To be consistent with the partition shape, we adopt Chebyshev distance to generate CM :

$$CM(p, q) = \max\left(\frac{h}{2}, \frac{w}{2}\right) - \max\left(|p - \frac{h}{2}|, |q - \frac{w}{2}|\right) \quad (10)$$

where (p, q) denotes the coordinates of pixels. Note that other distance metrics, *e.g.* Euclidean distance and Manhattan distance, will be compared in the experiments. The generation of $heat_i^{n_{SPS}}$ can be formulated as:

$$heat_i^{n_{SPS}} = (\mathcal{N}(\mathcal{M}(f_i^{n_{SPS}})) + CM_i^{n_{SPS}}) / 2 \quad (11)$$

where $\mathcal{N}(\cdot)$ denotes the normalization operation, and $\mathcal{M}(\cdot)$ denotes the average pooling operation. Next, we set a threshold δ to split the heatmap, resulting in a binary mask $Mask_i^{n_{SPS}}$:

$$Mask_i^{n_{SPS}}(p, q) = \begin{cases} 1, & heat_i^{n_{SPS}}(p, q) \geq \delta \\ 0, & heat_i^{n_{SPS}}(p, q) < \delta \end{cases} \quad (12)$$

Finally, in reference to FSRA [15], we leverage the value of $Mask_i^{n_{SPS}}$ to binary the input feature $f_i^{n_{SPS}}$, which can be expressed as follows:

$$\begin{cases} s_i^{n_{SPS}} = \mathcal{M}(\{f_i^{n_{SPS}}(p, q) | Mask_i^{n_{SPS}}(p, q) = 1\}) \\ b_i^{n_{SPS}} = \mathcal{M}(\{f_i^{n_{SPS}}(p, q) | Mask_i^{n_{SPS}}(p, q) = 0\}) \\ g_i^{n_{SPS}} = \mathcal{M}(f_i^{n_{SPS}}) \end{cases} \quad (13)$$

where $s_i^{n_{SPS}} \in \mathbb{R}^{2048 \times 1 \times 1}$ and $b_i^{n_{SPS}} \in \mathbb{R}^{2048 \times 1 \times 1}$ are denote the salient feature and background feature. We also utilize $g_i^{n_{SPS}} \in \mathbb{R}^{2048 \times 1 \times 1}$ to preserve the input information. It is worth mentioning that SGRS is implemented for each part-level features of both drone-view and satellite-view, resulting in $3N_{SPS}$ feature vectors.

C. Classification Supervision

We employ a classifier module to map feature vectors of all sources into one shared space. As shown in Fig. 4, the classifier module includes a fully connected layer (FC), a batch normalization layer (BN), a dropout layer (Dropout), and a classification layer (Cls). The process can be expressed as:

$$z_{i,j}^{n_{SPS}} = \mathcal{F}_{classifier}(j_i^{n_{SPS}}) \quad (14)$$

where $j \in \{g, s, b\}$ denotes the feature vector of different categories generated by Eq. (13).

Subsequently, we adopt a cross-entropy loss function to optimize our framework, with the objective of minimizing the distance between features of the same geo-tag:

$$\mathcal{L}_{CE} = \sum_{i,j,n_{SPS}} -\log\left(\frac{\exp(z_{i,j}^{n_{SPS}}(y))}{\sum_{c=1}^C \exp(z_{i,j}^{n_{SPS}}(c))}\right) \quad (15)$$

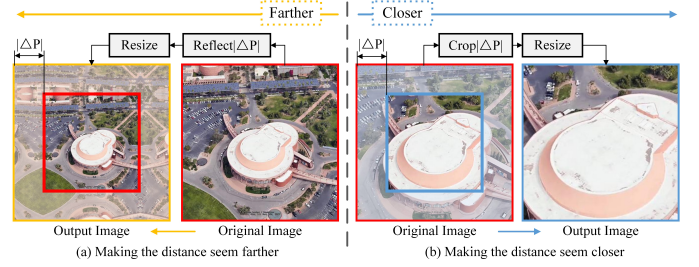


Fig. 5. The data augmentation strategy to extend the distance range of drone-views from the visual perspective. (a) Making the distance seem farther: given a drone image, mirror a strip ΔP pixels wide around the input image and resize it to initial resolution; (b) Making the distance seem closer: given a drone image, crop out a square ring ΔP pixels wide around the input image and resize it to initial resolution.

where $z_{i,j}^{n_{SPS}}(y)$ denotes the logit score of the ground-truth geo-tag y , and C denotes the number of geo-tag categories. It is noteworthy that the losses on the image of different part-level features are calculated independently.

IV. EXPERIMENTS

To evaluate the effectiveness of our DGDPL framework for UAV-view geo-localization, we conduct a series of experiments on University-1652 [8]. These experiments assess the performance of our method in terms of retrieval accuracy, robustness against scale variations, and the impact of both various components and hyper-parameters.

A. Datasets and Evaluation Metrics

Datasets. We perform extensive experiments based on the University-1652 [8] dataset for the following reasons: 1) the University-1652 contains diverse scenarios, including 1652 university buildings worldwide, where each building comprises 1 satellite-view image and 54 drone-view images. The training set includes 701 buildings of 33 universities, and the other 951 buildings of the remaining 39 universities are classified as the test set. 2) drone-view images exhibits considerable scale variation, with distances ranging from 123.5m to 256m (*i.e.*, $H_D \in [123.5m, 256m]$), supporting the verification of the anti-scale robustness of our DGDPL. Referring to LPN [20], the test set is equally divided into three parts according to the drone-view distance: **Long**, **Middle**, and **Short**. Then, comparing satellite-view images with UAV-view images, we set the value of H_S to 189.75m, which corresponds to the midpoint of the UAV distance range.

To further expand the distance range of drone-views, we design a data augmentation strategy to simulate more extreme image scales. As shown in Fig. 5, we introduce a parameter ΔP to adjust image scales (equivalent to UAV distance), which can be expressed as:

$$x_D^{\Delta P} = \mathcal{F}_{aug}(x_D; \Delta P) \quad (16)$$

where \mathcal{F}_{aug} denotes the process of data augmentation, x_D and $x_D^{\Delta P}$ denote the input image and synthesized image, respectively. ($\Delta P > 0$) means that making the distance of drone-view seem farther (see Fig. 5(a)), while ($\Delta P < 0$) means that making

TABLE I

COMPARISON WITH THE STATE-OF-THE-ART RESULTS REPORTED ON UNIVERSITY-1652. THE COMPARED METHOD ARE DIVIDED INTO TWO GROUPS, THE RESNET50-BASED METHODS AT THE TOP, AND THE ViT-BASED METHODS AT THE BOTTOM. BEST AND SECOND BEST PERFORMANCE ARE IN RED AND BLUE COLORS.

Methods	Publication	Backbone	Standard Test set		Short ($\Delta P=-100$)		Long ($\Delta P=100$)		Average	
			R@1	AP	R@1	AP	R@1	AP	R@1	AP
ResNet [72]	CVPR'16	ResNet-50	60.16	64.98	37.62	43.36	23.12	28.88	40.30	45.74
LPN [20]	TCSVT'21	ResNet-50	81.48	84.06	47.24	52.93	35.57	41.51	54.76	59.50
CA-HRS [73]	ACCV'22	ResNet-50	81.00	83.64	48.55	54.21	34.94	40.94	54.83	59.59
MCCG [9]	TCSVT'23	ResNet-50	70.94	75.04	34.54	40.60	25.06	31.25	43.51	48.96
Sample4Geo [33]	ICCV'23	ResNet-50	78.62	82.11	53.30	59.05	41.03	47.73	57.65	62.96
D^2 -GeM [12]	SPL'24	ResNet-50	84.49	86.81	55.55	60.92	37.30	43.48	59.11	63.73
DWDR(w.BT) [74]	TGRS'24	ResNet-50	71.79	75.71	49.16	54.75	37.24	43.90	52.73	58.12
DWDR(w.LPN) [74]	TGRS'24	ResNet-50	83.18	85.63	51.29	56.71	36.36	42.71	56.94	61.68
SDPL [50]	TCSVT'24	ResNet-50	85.19	87.43	60.24	65.10	48.29	54.32	64.57	68.95
DGDPL	-	ResNet-50	84.19	86.36	65.39	69.41	63.42	68.05	71.00	74.60
ViT [71]	ICLR'20	ViT-S	80.34	83.05	68.01	71.83	61.23	65.99	69.86	73.62
LPN [20]	TCSVT'21	ViT-S	87.07	88.91	69.62	73.48	69.81	73.98	75.50	78.79
FSRA [15]	TCSVT'21	ViT-S	85.10	87.19	71.48	75.17	65.67	70.04	74.08	77.46
SDPL [50]	TCSVT'24	ViT-S	85.57	87.61	68.90	72.76	70.56	74.65	75.01	78.34
DGDPL	-	ViT-S	88.08	89.77	75.12	78.33	78.15	81.34	80.45	83.14

the distance of drone-view seem closer (see Fig. 5(b)). $|\Delta P|$ denotes the degree of scale adjustment. Then, we roughly calculate the distance of synthesized image $x_D^{\Delta P}$:

$$H_D(x_D^{\Delta P}) = H_D(x_D) + \lambda_{aug} * \Delta P \quad (17)$$

where $\lambda_{aug}=0.7$ is the empirical value, estimated by the visual scale and distance of the existing drone-view images.

By applying the aforementioned strategy to **Long** and **Short** sets, we generate test sets with extreme scales, named as **Long**($\Delta P>0$) and **Short**($\Delta P<0$), respectively. Note that drone-views within the **Long**($\Delta P>0$) exhibit greater distances, whereas those within the **Short**($\Delta P<0$) have shorter distances.

Evaluation Metrics. To evaluate geo-localization performance, we employ Recall@K (R@K) and Average Precision (AP). R@K refers to the proportion of correctly matched images in the top-K of the ranking list, and AP measures the area under the Precision-Recall curve, considering the ranking of all positive images.

B. Model Settings and Training Details

Model Settings. For the default DGDPL framework, we set the feature map upsampling factor $\lambda=4$, the number of partitions to $N_{SPS}=4$, and partition scaling factor $\alpha=3.3$. For the SRGS, we adopt Chebyshev distance to generate coordinate map CM , and set the heatmap segmentation threshold $\delta=0.5$. For the University-1652 dataset, we roughly set drone-views distance $H_D \in [123.5m, 256m]$ and satellite-views distance $H_S=189.75m$, respectively.

Training Details. By default, we resize each input image to 512×512 for both training and testing phases, and employ the ResNet-50 [72] to extract visual features. In training, we set the initial learning rate of 0.001 for the backbone, and the rest of learnable parameters are set to 0.0001. Stochastic gradient descent (SGD) are adopted with batch size 4, momentum 0.9, and weight decay 0.0005 for optimization. The model are trained for 120 epochs, and the learning rate is decayed by 0.1 after 80 epochs. We also employ random horizontal

image flipping as data augmentation. During testing phase, Euclidean distance are adopted to measure the similarity between the query images and candidate images in the gallery set. Experiments are performed on an NVIDIA RTX 3090 GPU with 24 GB of memory.

C. Comparison with State-of-the-art

As shown in Table I, we compare the proposed DGDPL with other methods on University-1652. Except for the standard test set provided, we employ Eq. (16) to generate two supplementary test sets, named **Long**($\Delta P=100$) and **Short**($\Delta P=-100$), which exhibit more extreme distance of drone-views. In other words, **Long**($\Delta P=100$) and **Short**($\Delta P=-100$) have more significant cross-view scale differences. The quantitative results are divided into two groups, ResNet-based and ViT-based methods. On the ResNet-based track, DGDPL achieves 84.19% R@1 and 86.36% AP on default test set, 65.39% R@1 and 69.41% AP on **Short**($\Delta P=-100$) set and 63.42% R@1, and 68.05% AP on **Long**($\Delta P=100$) set, respectively. On the default test set, DGDPL achieves competitive performance with recent SPDL [50] and clearly outperforms other solutions, such as D^2 -GeM [12] and Sample4Geo [33]. Moreover, it is remarkable that our DGDPL yields superior results on both the **Short**($\Delta P=-100$) and **Long**($\Delta P=100$) compared with partition-based LPN [15] and SDPL [50]. Specifically, compared with LPN, DGDPL improves R@1 from 47.24%, 35.57% to 65.39% (+18.15%), 63.42% (+27.85%), respectively. On the ViT-based track, DGDPL is compatible with the ViT framework and has surpassed the state-of-the-art methods on **Short**($\Delta P=-100$) and **Long**($\Delta P=100$), achieving an average R@1 and AP of 80.45% and 83.14%. Compared with ViT [71] and FSRA, DGDPL significantly improves retrieval accuracy in all scenarios, with an average R@1 improvement of 10.59% and 6.37%. This shows that DGDPL is robust to scenes with inconsistent cross-view scales.

Moreover, we visualize some retrieved results in Fig. 6. To prove the anti-scaling robustness of DGDPL, we provide same numbered results generated by baseline [72] and LPN [20]

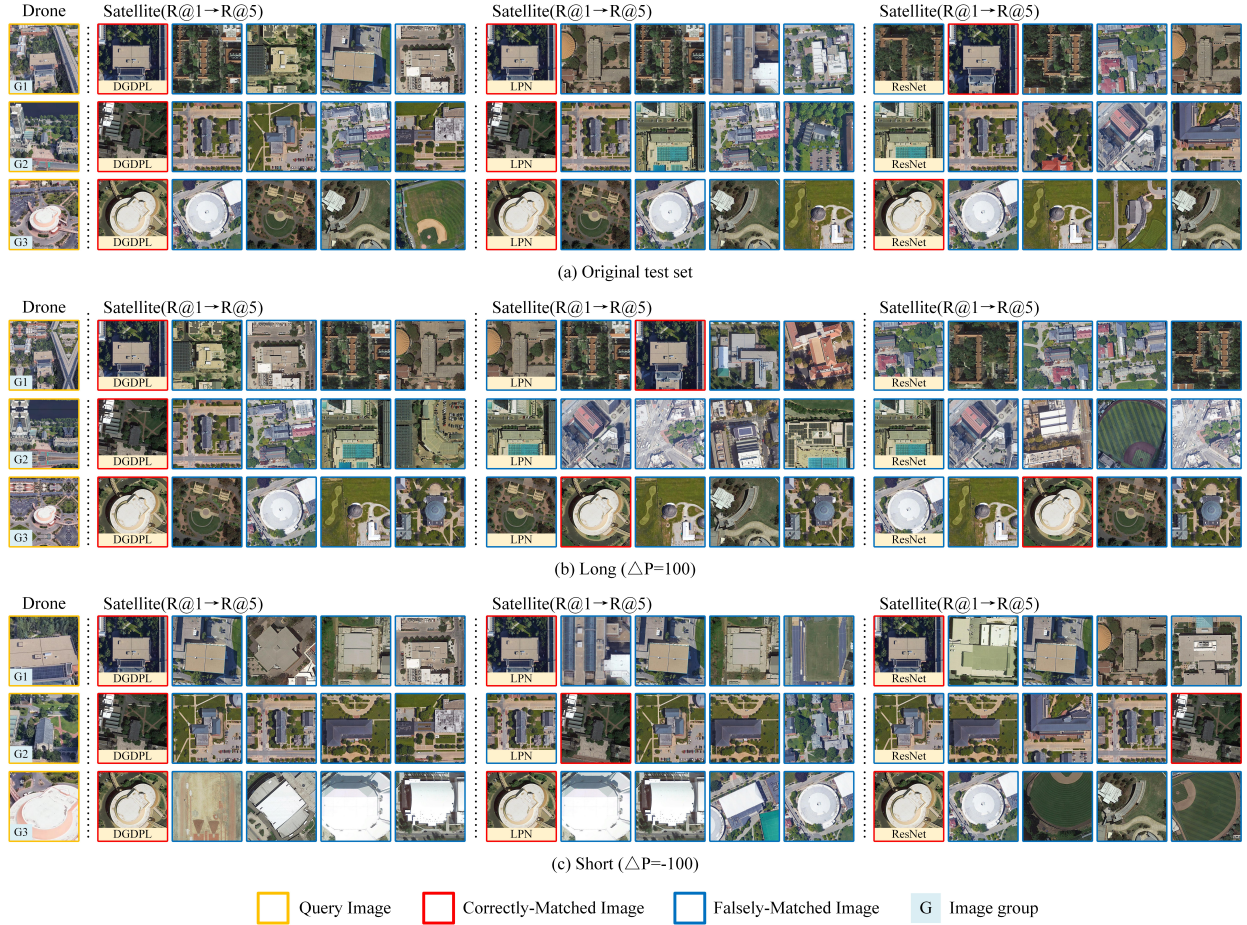


Fig. 6. Image retrieval results obtained with DGDPL, LPN and ResNet. Specifically, we present the correspondingly numbered image retrieval outcomes from the Test set (a), **Long**($\Delta P=100$)(b), and **Short**($\Delta P=-100$)(c), respectively.

on different test sets. For the original test set, both LPN and DGDPL are able to retrieve the correct satellite labels. As shown in Fig. 6(b) and (c), when the drone-view images undergo more drastic scale variations, it can be observed that our DGDPL still achieves correct results. This benefits from the fact that DGDPL explicitly aligns contents of partition pairs, thus mining robust contextual information. For example, as shown in Group 3 of Fig. 6(b), while the target in the satellite-view is discernible, the target size in the drone-view is notably smaller compared to that in the satellite-view. This discrepancy leads to a misalignment of features extracted by LPN with fixed templates, resulting in inaccurate retrieval results. On the other hand, as shown in Group 2 of Fig. 6(c), drone-view with shorter distance implies less environmental information and larger scale differences of cross-views. Compared to LPN, DGDPL can dynamically adjust partition sizes to boost the alignment of local features, but also refine part-level features, yielding accurate retrieval results.

D. Ablation Studies

To verify the effectiveness of DGDPL, we conduct extensive ablation studies, including:

- To validate the robustness of DGDPL in scale-inconsistent scenarios and its adaptability to diverse back-

bone networks;

- To prove the effectiveness of the proposed square partition strategy, distance-guided adjustment strategy and saliency-guided refinement strategy;
- To explore different variants of SGRS, including various CM , and output features;
- To Explore the effect of hyper-parameters on model performance, including number of partitions N_{SPS} , partition scaling factor α and input image size.

Robustness of DGDPL to scale-inconsistent scenarios.

As a hard-partition-based method, our DGDPL can alleviate the dependence on scale consistency of cross-views by dynamically adjusting the size of partition pairs. To fully verify the robustness of DGDPL for scale-inconsistent scenarios, we first synthesize a series of test sets with closer and longer distance of drone-views, named **Short**($\Delta P < 0$) and **Long**($\Delta P > 0$), where a larger $|\Delta P|$ represents a larger UAV-view scale variation. Then we compare the proposed DGDPL with representative partition-based methods, such as LPN [20] and FSRA [15]. The results are shown in Table II, divided into ResNet50-based track and ViT-based track. The performance degradation of each method on different datasets is shown in Fig. 7. On the ResNet50-based track, DGDPL shows the best retrieval accuracy, with significantly less performance

TABLE II

ABLATION STUDY ON ROBUSTNESS OF DGDPL TO SCALE-INCONSISTENT SCENARIOS. WE REPORTED THE R@1 ACCURACY FOR BASELINE, LPN, FSRA, SDPL AND DGDPL ON VARIOUS TEST SETS. THE EXPERIMENTAL RESULTS ARE DIVIDED INTO TWO GROUPS: RESNET50-BASED AT THE TOP AND ViT-BASED AT THE BOTTOM. BEST AND SECOND BEST PERFORMANCE ARE IN RED AND BLUE COLORS, RESPECTIVELY.

Test sets	Short($\Delta P \leq 0$)						Middle	Long($\Delta P \geq 0$)						Average
	-150	-100	-75	-50	-25	0	-	0	+25	+50	+75	+100	+150	
ResNet-50 [72]	9.26	37.62	48.40	56.19	61.27	64.81	63.58	52.07	40.40	33.82	27.88	23.12	16.25	41.12
FSRA [15]	7.39	33.24	46.18	54.51	59.87	64.15	65.07	48.41	36.50	29.43	24.53	20.95	26.51	39.74
LPN [20]	9.73	47.24	64.19	74.82	80.49	84.11	86.30	74.01	59.38	49.58	41.20	35.57	28.31	56.53
SDPL [50]	19.36	60.24	72.30	79.25	83.85	86.39	88.56	80.58	69.92	62.25	54.76	48.29	39.57	65.02
DGDPL(w/o DGAS)	20.56	60.08	72.33	78.89	82.52	84.75	86.27	79.63	70.77	64.24	57.63	51.13	39.34	65.24
DGDPL	24.84	65.39	75.61	80.70	83.41	85.01	85.72	81.87	75.34	71.19	67.17	63.42	55.64	70.40
ViT-S [71]	41.06	68.01	74.39	77.96	79.77	80.49	81.87	78.66	72.98	69.16	65.73	61.23	54.45	69.67
FSRA [15]	39.35	71.48	78.71	82.94	84.44	85.45	86.39	83.44	78.86	74.73	70.72	65.67	57.26	73.80
LPN [20]	32.93	69.62	78.32	83.13	85.97	87.11	88.41	85.71	81.33	78.12	73.80	69.81	62.01	75.09
SDPL [50]	33.93	68.90	77.22	82.07	84.62	85.45	86.99	84.27	80.27	77.59	74.24	70.56	63.72	74.60
DGDPL(w/o DGAS)	38.79	73.66	80.66	84.39	86.59	87.34	89.01	87.46	84.05	81.13	78.01	74.66	66.20	77.84
DGDPL	41.15	75.12	81.46	85.18	87.03	87.70	89.06	87.47	85.22	82.97	80.61	78.15	72.33	79.46

degradation than other partition-based methods. In particular, compared with LPN and SDPL, our DGDPL improves average R@1 from 56.53%, 65.02% to 70.40%(+13.87%, +5.38%), respectively. Furthermore, the integration of DGAS into the DGDPL framework led to a notable improvement in retrieval accuracy in extreme scenarios, with a 5.16% improvement in the average R@1. This highlights that DGAS facilitates alignment of fine-grained features from multiple views. On the ViT-based track, DGDPL also achieves optimal retrieval accuracy across datasets of all scales, with an average R@1 of 79.46%. Compared with FSRA and LPN, DGDPL improves average R@1 by 5.66% and 4.37%. This fully demonstrates the robustness of DGDPL to cross-view scale variations, as well as the compatibility with various backbone networks. Moreover, Fig. 7 proves that DGAS can alleviate the performance degradation of DGDPL caused by cross-view scale inconsistency without additional learnable parameters. It is worth noting that the performance degradation of ViT-based methods is generally lower than that of ResNet-based methods. We conclude that the ViT framework is capable of capturing long-range feature dependencies, thereby contributing to its robustness against scale changes. As depicted in Fig. 7(c), in contrast to ResNet-based methods, the performance degradation of ViT methods is comparable in **Short**($\Delta P < 0$), whereas the baseline exhibits the minimal degradation. This phenomenon can be primarily attributed to the robust feature extraction capability of the ViT, coupled with the scarcity of effective features in **Short**($\Delta P < 0$) scenarios.

Effectiveness of each component. The core components of DGDPL are SPS, DGAS and SGRS. We construct five derived models to validate the effectiveness of each strategy, and results are shown in Table III. Firstly, fine-grained partitions generated by SPS contain both local and global features, thus learning rich contextual information. Compared to the baseline, SPS provides +19.76% R@1, +21.60% R@1 and +24.88% R@1 on three test sets. When DGAS is combined with SPS, the model’s accuracy is notably enhanced in scenarios involving scale inconsistency, while maintaining stable performance in the standard test set. For instance, upon removing DGAS from DGDPL, the R@1 of model(SPS+SGRS) decreases by 0.65%, 5.31%, and 12.29% on Standard test set, **Short**($\Delta P = -100$) and **Long**($\Delta P = 100$), respectively. We

TABLE III

PERFORMANCE COMPARISON OF DGDPL FRAMEWORK WITH DIFFERENT COMPONENTS. ✓ INDICATES THAT THE MODULE IS APPLIED.

Model structure			Standard Test set		Short($\Delta P = -100$)		Long($\Delta P = 100$)	
SPS	DGAS	SGRS	R@1	AP	R@1	AP	R@1	AP
			60.16	64.98	37.62	43.36	23.12	28.88
			79.92	82.58	59.22	63.80	48.00	53.64
✓			80.69	83.35	59.75	64.17	60.71	65.56
✓			83.54	85.84	60.08	64.62	51.13	56.98
✓	✓	✓	84.19	86.36	65.39	69.41	63.42	68.05

emphasize that drone-views with short distances contain incomplete depictions of targets and limited environmental information. consequently, it is plausible that the performance gain of the DGAS is lower in the **Short** set compared to the **Long** set. To further improve the retrieval accuracy of DGDPL, we introduce SGRS to refine salient regions of partitions. It can be observed that SGRS boosts the retrieval accuracy of DGDPL in various scenarios, yielding 3.50%, 5.64% and 2.71% R@1 improvement over the model(SPS+DGAS).

Variants of SGRS. As mentioned above, SGRS segments part-level features based on heatmaps to obtain global features, salient features and background features, which are matched independently. To fully verify the effectiveness of SGRS, we construct a variety of SGRS variants, including different output combinations as well as coordinate map CM , as shown in Fig. 8. Table IV shows the experimental results. Regardless of the specific combination of output modes employed by the SGRS to refine partitions, it consistently outperforms the model without SGRS (*i.e.*, only g_i). On the other hand, compared to Euclidean distance and Manhattan distance, the utilization of Chebyshev distance within SGRS yields an optimal gain, surpassing that of Manhattan distance by a notable margin. This phenomenon can be attributed to the fact that the CM generated by the Chebyshev paradigm exhibits a structural similarity to the square partition strategy employed. Therefore, it is within the realm of expectation that the model based on Euclidean distance yields comparable results. Since the feature segmentation process of SGRS is unsupervised, the injected CM can assist SGRS in judging the importance of features and classifying neighborhood features into the same class. Upon removal of the CM from SGRS, the average R@1 and AP metrics of the DGDPL decreased by 6.37% and 5.72%.

partition scaling factor α . Referring to Eq (4), our

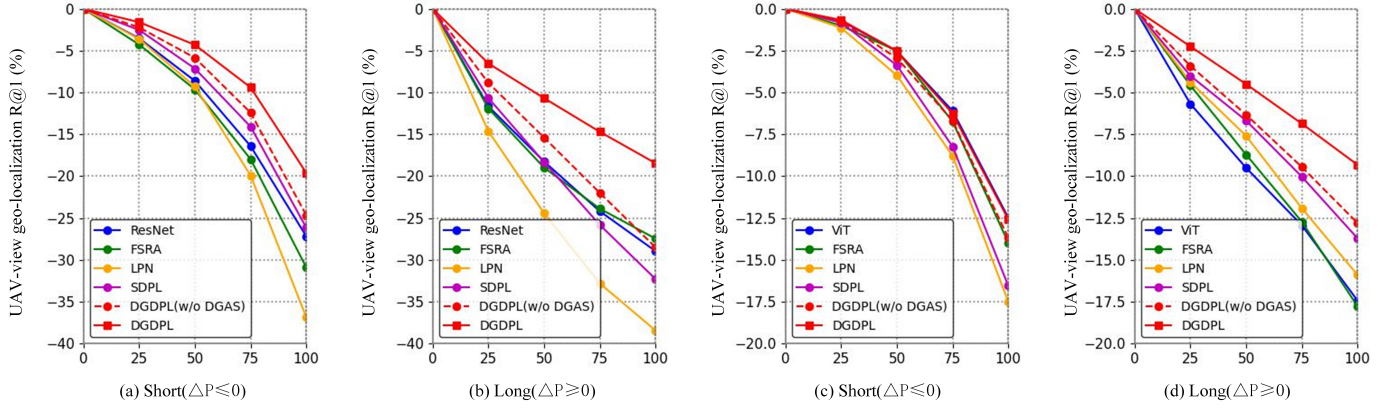


Fig. 7. Performance degradation of different methods on **Short**($\Delta P \leq 0$) and **Long**($\Delta P \geq 0$). Vertical axis: magnitude of decrease in R@1. Horizontal axis: degree of distance adjustment $|\Delta P|$. (a) and (b) show the results of ResNet-based methods, while (c) and (d) show the results of ViT-based methods.

TABLE IV

ABLATION STUDY ON DIFFERENT VARIANTS OF SGRS. THE EXPERIMENT AIMS TO EXPLORE THE IMPACT OF DIFFERENT FEATURE COMBINATIONS AND COORDINATE MAPS ON PERFORMANCE.

Output features			Coordinate maps			Standard Test set		Short ($\Delta P=-100$)		Long ($\Delta P=100$)		Average	
g_i	s_i	b_i	Euclidean	Manhattan	Chebyshev	R@1	AP	R@1	AP	R@1	AP	R@1	AP
✓						80.69	83.35	59.75	64.17	60.71	65.56	67.05	71.02
✓	✓				✓	82.15	84.57	64.36	68.36	62.00	66.72	69.50	73.21
✓		✓			✓	83.56	85.88	62.37	66.70	61.55	66.36	69.16	72.98
	✓	✓			✓	83.99	86.14	63.57	67.82	61.49	66.19	69.68	73.38
✓	✓					79.66	82.42	56.38	61.51	57.87	62.72	64.63	68.88
✓	✓	✓	✓			84.02	86.20	64.16	68.40	63.16	67.69	70.44	74.09
✓	✓	✓		✓		82.69	85.05	59.15	63.73	60.76	65.71	67.53	71.49
✓	✓	✓			✓	84.19	86.36	65.39	69.41	63.42	68.05	71.00	74.60

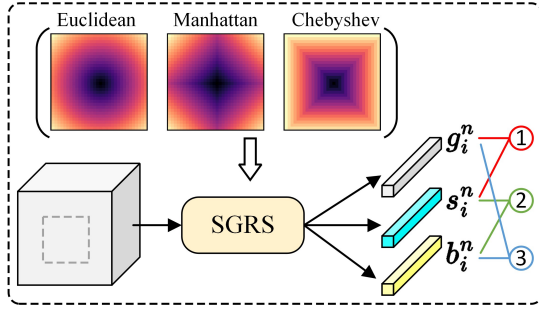


Fig. 8. Variants of SGRS in ablation experiments. Coordinate map (CM) can be calculated by Euclidean distance, Manhattan distance or Chebyshev distance. The default SRM output contains global features (g_i^n), salient features (s_i^n), and background features (b_i^n). The remaining three output modes can be obtained by combining them in pairs, *i.e.*, ① $g_i^n + s_i^n$, ② $s_i^n + b_i^n$, ③ $g_i^n + b_i^n$.

DGAS can adjust the degree of variation in partition size by modifying α . An improperly choice for α may result in a misalignment of content between cross-view partition pairs. We set a series of α for experiments, and the results are shown in Table V. It can be observed that when α is small, the size of partition pairs of DGDPL is almost of the same size, yielding favorable outcomes in the **Middle** set but suffering from significant performance degradation in extreme scenarios. When α increases from 0.0 to 3.3, the retrieval accuracy of DGDPL continues to rise in the **Short**($\Delta P \leq 0$) and **Long**($\Delta P \geq 0$) sets. In particular, the R@1 of our method improves from 17.84% and 34.93% to

24.84%(+7.00%) and 55.64%(+20.71%) on **Short**($\Delta P=-150$) set and **Long**($\Delta P=+150$) set, respectively. The average R@1 of DGDPL also increases from 63.83% to 70.40%(+6.57%). This verifies that DGAS can enhance the robustness of our model against scale changes. As α continues to increase, the retrieval accuracy of DGDPL exhibits a slight decline across various **Short**($\Delta P \leq 0$) scenes. Considering the average performance of the model, we set $\alpha=3.3$ as the default setting.

Number of partitions. The number of parts N_{SPS} is a key hyper-parameter in our DGDPL. As shown in Table VI, we report the quantitative results of DGDPL with different N_{SPS} on the three test-sets. As the number of parts increases, the retrieval accuracy of DGDPL exhibits a gradual enhancement, particularly in scenarios involving inconsistent scales. For example, when N_{SPS} increases from 1 to 3, DGDPL improves R@1 by 12.58%, 18.87% and 30.96% in the standard test set, **Short**($\Delta P=-100$) and **Long**($\Delta P=-100$), respectively. Further increasing N_{SPS} , the retrieval performance of DGDPL tends to be stable with a slight improvement, because 3 or 4 partitions are enough to exploit rich contextual information. As the basic component of DGDPL, our SPS divides high-level features into fixed-size fine-grained partitions. To thoroughly demonstrate the anti-scaling robustness of SPS, we also report results for LPN [20] and SPS under various number of partitions, as shown in Fig. 9. It is evident that our SPS exhibits comparable performance to the LPN on the standard test set, while outperforming LPN significantly in scale-inconsistent scenarios. When SPS meets DGAS and SGRS, model (*i.e.*, DGDPL) with various N_{SPS} achieves significant performance

TABLE V

PERFORMANCE COMPARISON OF DGDPL WITH VARIOUS PARTITION SCALING FACTOR α . WE REPORTED THE R@1 ACCURACY ON THREE TYPES OF DATASETS, INCLUDING **SHORT**($\Delta P \leq 0$) SET, **MIDDLE** SET AND **LONG**($\Delta P \geq 0$) SET.

Test sets	Short ($\Delta P \leq 0$)					Middle	Long ($\Delta P \geq 0$)					Average		
	-150	-100	-75	-50	-25		0	0	+25	+50	+75		+100	+150
$\alpha=0.0$	17.84	58.84	71.64	78.86	83.12	85.31	86.36	78.79	69.52	62.24	54.71	47.69	34.93	63.83
$\alpha=0.5$	21.55	62.64	73.37	79.00	83.02	85.20	86.73	79.46	69.87	63.84	57.98	52.21	40.51	65.79
$\alpha=1.5$	23.69	63.57	74.08	80.36	83.98	85.44	86.31	80.11	72.49	67.29	62.14	56.59	46.20	67.86
$\alpha=2.5$	25.66	64.66	74.67	80.28	83.44	85.10	86.13	80.61	73.46	68.99	64.02	58.82	50.20	68.92
$\alpha=3.3$	24.84	65.39	75.61	80.70	83.41	85.01	85.72	81.87	75.34	71.19	67.17	63.42	55.64	70.40
$\alpha=4.0$	26.12	64.73	74.45	79.74	82.63	84.27	84.87	80.67	74.73	71.35	67.83	64.42	56.77	70.19

TABLE VI

PERFORMANCE COMPARISON OF DGDPL WITH DIFFERENT NUMBER OF PARTS. N_{SPS} DENOTES THE NUMBER OF PARTS GENERATED BY *SPS*.

Numbers N_{SPS}	Standard Test set		Short ($\Delta P=-100$)		Long ($\Delta P=100$)	
	R@1	AP	R@1	AP	R@1	AP
1	71.54	75.35	46.66	52.41	31.05	36.90
2	80.83	83.49	57.36	62.03	50.99	56.56
3	84.12	86.31	65.23	69.26	62.01	66.88
4	84.19	86.36	65.39	69.41	63.42	68.05

TABLE VII

PERFORMANCE COMPARISON OF DGDPL WITH DIFFERENT INPUT IMAGE SIZE.

Image size	Standard Test set		Short ($\Delta P=-100$)		Long ($\Delta P=100$)	
	R@1	AP	R@1	AP	R@1	AP
224×224	74.79	78.01	48.32	53.75	37.53	43.59
256×256	77.14	80.16	54.30	59.50	40.58	46.51
320×320	81.08	83.74	65.51	61.66	47.68	53.22
384×384	82.92	85.27	65.08	69.28	54.69	59.84
512×512	84.19	86.36	65.39	69.41	63.42	68.05

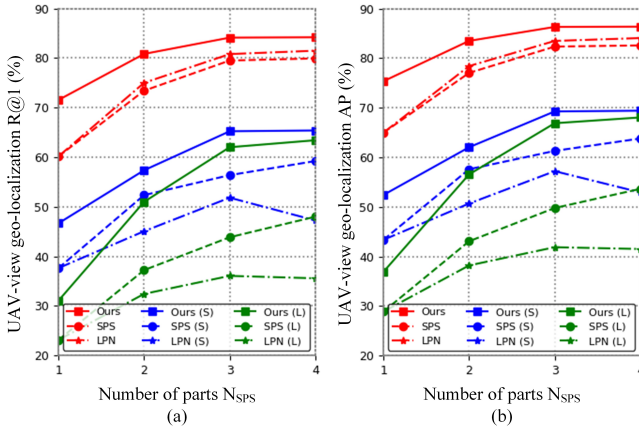


Fig. 9. Comparison of LPN, SPS and DGDPL with different numbers of parts. The experiments were conducted on the standard test set, **Short**($\Delta P=-100$) and **Long**($\Delta P=100$).

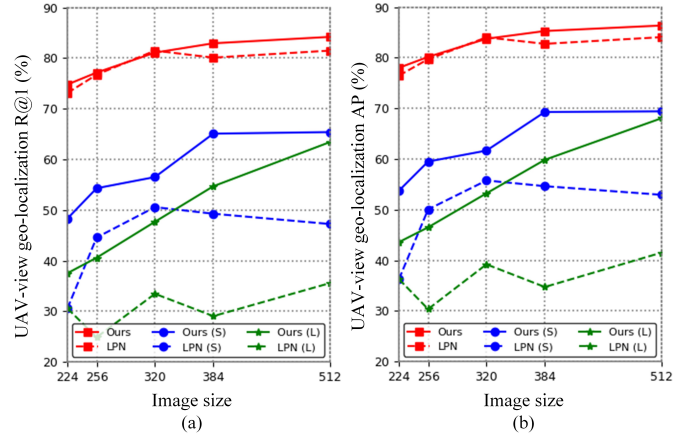


Fig. 10. Impact of different input sizes on R@1 and AP. The experiments were conducted on the standard test set, **Short**($\Delta P=-100$) and **Long**($\Delta P=100$).

improvement in each test set.

input image size. A small training size compresses the fine-grained information of the input image, thus compromising the discriminative representation learning. We selected five input image resolutions to investigate the impact of input image size on model performance. To guarantee that the partition resolution remains positive, we adjust the scaling factor α in accordance with variations in the input image resolution. As shown in Table VII, when the input image resolution changes from 224 to 512, model performance improves continuously on multiple datasets. Furthermore, with the image resolution increasing from 320 to 512, the gain of DGDPL is 3.11% on the standard test set, while the improvement is 8.88% and 15.74% on **Short**($\Delta P=-100$) and **Long**($\Delta P=100$), respectively. We also present the results of LPN [20], the most relevant study, under different input picture sizes, as depicted in Fig. 10. With the increase of image resolution, the accuracy of LPN and DGDPL is equivalent in the standard test set, but the performance gap between them gradually widens in extreme scenes. It can also be found that the performance

of LPN is unstable in **Short**($\Delta P=-100$) and **Long**($\Delta P=100$). This indicates that DGDPL can extract the rich fine-grained information contained in high-resolution images.

V. CONCLUSIONS

In this paper, we study the UAV-view geo-localization in scale-inconsistent scenarios, and propose a simple and effective part-based representation learning framework called DGDPL. Specifically, we introduce a square partition strategy to capture fine-grained features while retaining the global structure. Adhering to the rule that objects in UAV-views appear larger when closer and smaller when farther, we further introduce a distance-guided adjustment strategy. Based on the distance ratio of cross-views, we dynamically adjust the partition size of the UAV branch to promote the content consistency of partition pairs, thereby achieving accurate cross-view matching against scale variations. Moreover, we explore a saliency-guided refinement strategy to refine part-level features into salient features and background features, further

improving cross-view image matching performance without compromising the robustness of our model to scale variations. Extensive experiments on the University-1652 demonstrate that the robustness of our method in various scale-inconsistent scenarios. Ablation experiments show that DGDPL reveals satisfactory compatibility with various backbone networks. In the future, we plan to collect a real-world dataset containing UAV pose information to drive real-world cross-view matching, such as UAV-view geo-localization and UAV self-positioning.

REFERENCES

- [1] P. Goodrich, O. Betancourt, A. C. Arias, and T. Zohdi, "Placement and drone flight path mapping of agricultural soil sensors using machine learning," *Computers and Electronics in Agriculture*, vol. 205, p. 107591, 2023.
- [2] M. A. Khan, W. Ectors, T. Bellemans, D. Janssens, and G. Wets, "Uav-based traffic analysis: A universal guiding framework based on literature survey," *Transportation research procedia*, vol. 22, pp. 541–550, 2017.
- [3] L. Zhao and M. Zhu, "Ms-yolov7: Yolov7 based on multi-scale for object detection on uav aerial photography," *Drones*, vol. 7, no. 3, p. 188, 2023.
- [4] F. Zimmermann, C. Eling, L. Klingbeil, and H. Kuhlmann, "Precise positioning of uavs—dealing with challenging rtk-gps measurement conditions during automated uav flights," *ISPRS Annals of the Photogrammetry, Remote Sensing and Spatial Information Sciences*, vol. 4, pp. 95–102, 2017.
- [5] T.-Y. Lin, S. Belongie, and J. Hays, "Cross-view image geolocalization," in *Proceedings of the IEEE Conference on Computer Vision and Pattern Recognition*, 2013, pp. 891–898.
- [6] M. Bansal, H. S. Sawhney, H. Cheng, and K. Daniilidis, "Geo-localization of street views with aerial image databases," in *Proceedings of the 19th ACM international conference on Multimedia*, 2011, pp. 1125–1128.
- [7] F. Castaldo, A. Zamir, R. Angst, F. Palmieri, and S. Savarese, "Semantic cross-view matching," in *Proceedings of the IEEE International Conference on Computer Vision Workshops*, 2015, pp. 9–17.
- [8] Z. Zheng, Y. Wei, and Y. Yang, "University-1652: A multi-view multi-source benchmark for drone-based geo-localization," in *Proceedings of the 28th ACM international conference on Multimedia*, 2020, pp. 1395–1403.
- [9] T. Shen, Y. Wei, L. Kang, S. Wan, and Y.-H. Yang, "Mccg: A convnext-based multiple-classifier method for cross-view geo-localization," *IEEE Transactions on Circuits and Systems for Video Technology*, 2023.
- [10] J. Lin, Z. Zheng, Z. Zhong, Z. Luo, S. Li, Y. Yang, and N. Sebe, "Joint representation learning and keypoint detection for cross-view geo-localization," *IEEE Transactions on Image Processing*, vol. 31, pp. 3780–3792, 2022.
- [11] T. Wang, Z. Zheng, Z. Zhu, Y. Sun, C. Yan, and Y. Yang, "Learning cross-view geo-localization embeddings via dynamic weighted decorrelation regularization," *IEEE Transactions on Geoscience and Remote Sensing*, 2024.
- [12] T. Wang, Z. Yang, Q. Chen, Y. Sun, and C. Yan, "Rethinking pooling for multi-granularity features in aerial-view geo-localization," *IEEE Signal Processing Letters*, 2024.
- [13] C. Zheng, A. Shrivastava, and A. Owens, "Exif as language: Learning cross-modal associations between images and camera metadata," in *Proceedings of the IEEE/CVF Conference on Computer Vision and Pattern Recognition*, 2023, pp. 6945–6956.
- [14] C. Zheng, J. Zhang, A. Kembhavi, and R. Krishna, "Iterated learning improves compositionality in large vision-language models," in *Proceedings of the IEEE/CVF Conference on Computer Vision and Pattern Recognition*, 2024, pp. 13 785–13 795.
- [15] M. Dai, J. Hu, J. Zhuang, and E. Zheng, "A transformer-based feature segmentation and region alignment method for uav-view geo-localization," *IEEE Transactions on Circuits and Systems for Video Technology*, vol. 32, no. 7, pp. 4376–4389, 2021.
- [16] H. Zhao, K. Ren, T. Yue, C. Zhang, and S. Yuan, "Transfg: A cross-view geo-localization of satellite and uavs imagery pipeline using transformer-based feature aggregation and gradient guidance," *IEEE Transactions on Geoscience and Remote Sensing*, 2024.
- [17] Q. Li, X. Yang, J. Fan, R. Lu, B. Tang, S. Wang, and S. Su, "Geoformer: An effective transformer-based siamese network for uav geo-localization," *IEEE Journal of Selected Topics in Applied Earth Observations and Remote Sensing*, 2024.
- [18] S. Li, C. Liu, H. Qiu, and Z. Li, "A transformer-based adaptive semantic aggregation method for uav visual geo-localization," in *Chinese Conference on Pattern Recognition and Computer Vision (PRCV)*. Springer, 2023, pp. 465–477.
- [19] S. Zhu, M. Shah, and C. Chen, "Transgeo: Transformer is all you need for cross-view image geo-localization," in *Proceedings of the IEEE/CVF Conference on Computer Vision and Pattern Recognition*, 2022, pp. 1162–1171.
- [20] T. Wang, Z. Zheng, C. Yan, J. Zhang, Y. Sun, B. Zheng, and Y. Yang, "Each part matters: Local patterns facilitate cross-view geo-localization," *IEEE Transactions on Circuits and Systems for Video Technology*, vol. 32, no. 2, pp. 867–879, 2022.
- [21] H. Li, Q. Chen, Z. Yang, and J. Yin, "Drone satellite matching based on multi-scale local pattern network," in *Proceedings of the 2023 Workshop on UAVs in Multimedia: Capturing the World from a New Perspective*, 2023, pp. 51–55.
- [22] H. Li, T. Wang, Q. Chen, Q. Zhao, S. Jiang, C. Yan, and B. Zheng, "Aerial-view geo-localization based on multi-layer local pattern cross-attention network," *Applied Intelligence*, vol. 54, no. 21, pp. 11 034–11 053, 2024.
- [23] F. Ge, Y. Zhang, L. Wang, W. Liu, Y. Liu, S. Coleman, and D. Kerr, "Multi-level feedback joint representation learning network based on adaptive area elimination for cross-view geo-localization," *IEEE Transactions on Geoscience and Remote Sensing*, 2024.
- [24] F. Ge, Y. Zhang, Y. Liu, G. Wang, S. Coleman, D. Kerr, and L. Wang, "Multibranch joint representation learning based on information fusion strategy for cross-view geo-localization," *IEEE Transactions on Geoscience and Remote Sensing*, vol. 62, pp. 1–16, 2024.
- [25] C. Nanhua, T.-s. LOU, and Z. Liangyu, "Mmhca: Multi-feature representations based on multi-scale hierarchical contextual aggregation for uav-view geo-localization," *Chinese Journal of Aeronautics*, 2024.
- [26] Y. Chen, Z. Yang, and Q. Chen, "A cross-view matching method based on dense partition strategy for uav geolocalization," in *Proceedings of the 2023 Workshop on UAVs in Multimedia: Capturing the World from a New Perspective*, ser. UAVM '23, 2023, p. 19–23.
- [27] J. Zhuang, M. Dai, X. Chen, and E. Zheng, "A faster and more effective cross-view matching method of uav and satellite images for uav geolocalization," *Remote Sensing*, vol. 13, no. 19, p. 3979, 2021.
- [28] J. Shao and L. Jiang, "Style alignment-based dynamic observation method for uav-view geo-localization," *IEEE Transactions on Geoscience and Remote Sensing*, vol. 61, pp. 1–14, 2023.
- [29] S. Workman and N. Jacobs, "On the location dependence of convolutional neural network features," in *Proceedings of the IEEE Conference on Computer Vision and Pattern Recognition Workshops*, 2015, pp. 70–78.
- [30] S. Workman, R. Souvenir, and N. Jacobs, "Wide-area image geolocalization with aerial reference imagery," in *Proceedings of the IEEE International Conference on Computer Vision*, 2015, pp. 3961–3969.
- [31] M. Zhai, Z. Bessinger, S. Workman, and N. Jacobs, "Predicting ground-level scene layout from aerial imagery," in *Proceedings of the IEEE Conference on Computer Vision and Pattern Recognition*, 2017, pp. 867–875.
- [32] L. Liu and H. Li, "Lending orientation to neural networks for cross-view geo-localization," in *Proceedings of the IEEE/CVF conference on computer vision and pattern recognition*, 2019, pp. 5624–5633.
- [33] F. Deuser, K. Habel, and N. Oswald, "Sample4geo: Hard negative sampling for cross-view geo-localisation," in *Proceedings of the IEEE/CVF International Conference on Computer Vision*, 2023, pp. 16 847–16 856.
- [34] X. Zhang, X. Li, W. Sultani, Y. Zhou, and S. Wshah, "Cross-view geo-localization via learning disentangled geometric layout correspondence," in *Proceedings of the AAAI Conference on Artificial Intelligence*, vol. 37, no. 3, 2023, pp. 3480–3488.
- [35] S. Zhu, T. Yang, and C. Chen, "Vigor: Cross-view image geo-localization beyond one-to-one retrieval," in *Proceedings of the IEEE/CVF Conference on Computer Vision and Pattern Recognition*, 2021, pp. 3640–3649.
- [36] B. Clark, A. Kerrigan, P. P. Kulkarni, V. V. Cepeda, and M. Shah, "Where we are and what we're looking at: Query based worldwide image geo-localization using hierarchies and scenes," in *Proceedings of the IEEE/CVF Conference on Computer Vision and Pattern Recognition*, 2023, pp. 23 182–23 190.
- [37] G. Li, M. Qian, and G.-S. Xia, "Unleashing unlabeled data: A paradigm for cross-view geo-localization," in *Proceedings of the IEEE/CVF Con-*

- ference on *Computer Vision and Pattern Recognition*, 2024, pp. 16719–16729.
- [38] A. Tokor, Q. Zhou, M. Maximov, and L. Leal-Taixé, “Coming down to earth: Satellite-to-street view synthesis for geo-localization,” in *Proceedings of the IEEE/CVF Conference on Computer Vision and Pattern Recognition*, 2021, pp. 6488–6497.
- [39] Y. Shi, D. Campbell, X. Yu, and H. Li, “Geometry-guided street-view panorama synthesis from satellite imagery,” *IEEE Transactions on Pattern Analysis and Machine Intelligence*, vol. 44, no. 12, pp. 10009–10022, 2022.
- [40] W. Li, J. He, J. Ye, H. Zhong, Z. Zheng, Z. Huang, D. Lin, and C. He, “Crossviewdiff: A cross-view diffusion model for satellite-to-street view synthesis,” *arXiv preprint arXiv:2408.14765*, 2024.
- [41] R. Zhu, L. Yin, M. Yang, F. Wu, Y. Yang, and W. Hu, “Sues-200: A multi-height multi-scene cross-view image benchmark across drone and satellite,” *IEEE Transactions on Circuits and Systems for Video Technology*, 2023.
- [42] M. Dai, E. Zheng, Z. Feng, L. Qi, J. Zhuang, and W. Yang, “Vision-based uav self-positioning in low-altitude urban environments,” *IEEE Transactions on Image Processing*, 2023.
- [43] Y. Ji, B. He, Z. Tan, and L. Wu, “Game4loc: A uav geo-localization benchmark from game data,” *arXiv preprint arXiv:2409.16925*, 2024.
- [44] Q. Ye, J. Luo, and Y. Lin, “A coarse-to-fine visual geo-localization method for gnss-denied uav with oblique-view imagery,” *ISPRS Journal of Photogrammetry and Remote Sensing*, vol. 212, pp. 306–322, 2024.
- [45] H. Li, C. Xu, W. Yang, H. Yu, and G.-S. Xia, “Learning cross-view visual geo-localization without ground truth,” *arXiv preprint arXiv:2403.12702*, 2024.
- [46] Q. He, A. Xu, Y. Zhang, Z. Ye, W. Zhou, R. Xi, and Q. Lin, “A contrastive learning based multiview scene matching method for uav view geo-localization,” *Remote Sensing*, vol. 16, no. 16, p. 3039, 2024.
- [47] B. Sun, G. Liu, and Y. Yuan, “F3-net: Multi-view scene matching for drone-based geo-localization,” *IEEE Transactions on Geoscience and Remote Sensing*, 2023.
- [48] Z. Wang, D. Shi, C. Qiu, S. Jin, T. Li, Y. Shi, Z. Liu, and Z. Qiao, “Sequence matching for image-based uav-to-satellite geolocalization,” *IEEE Transactions on Geoscience and Remote Sensing*, 2024.
- [49] X. Liu, Z. Wang, Y. Wu, and Q. Miao, “Segcn: A semantic-aware graph convolutional network for uav geo-localization,” *IEEE Journal of Selected Topics in Applied Earth Observations and Remote Sensing*, 2024.
- [50] Q. Chen, T. Wang, Z. Yang, H. Li, R. Lu, Y. Sun, B. Zheng, and C. Yan, “Sdpl: Shifting-dense partition learning for uav-view geo-localization,” *IEEE Transactions on Circuits and Systems for Video Technology*, pp. 1–1, 2024.
- [51] X. Tian, J. Shao, D. Ouyang, and H. T. Shen, “Uav-satellite view synthesis for cross-view geo-localization,” *IEEE Transactions on Circuits and Systems for Video Technology*, vol. 32, no. 7, pp. 4804–4815, 2021.
- [52] J. Sun, H. Sun, L. Lei, K. Ji, and G. Kuang, “Tirsa: A three stage approach for uav-satellite cross-view geo-localization based on self-supervised feature enhancement,” *IEEE Transactions on Circuits and Systems for Video Technology*, 2024.
- [53] Z. Cui, P. Zhou, X. Wang, Z. Zhang, Y. Li, H. Li, and Y. Zhang, “A novel geo-localization method for uav and satellite images using cross-view consistent attention,” *Remote Sensing*, vol. 15, no. 19, p. 4667, 2023.
- [54] F. Deuser, M. Werner, K. Habel, and N. Oswald, “Optimizing geo-localization with k-means re-ranking in challenging weather conditions,” in *Proceedings of the 2nd Workshop on UAVs in Multimedia: Capturing the World from a New Perspective*, 2024, pp. 9–13.
- [55] Y. Yan, C. Liu, C. Chen, X. Sun, L. Jin, X. Peng, and X. Zhou, “Fine-grained attention and feature-sharing generative adversarial networks for single image super-resolution,” *IEEE Transactions on Multimedia*, vol. 24, pp. 1473–1487, 2021.
- [56] S. Ding, Q. Wang, L. Guo, X. Li, L. Ding, and X. Wu, “Wavelet and adaptive coordinate attention guided fine-grained residual network for image denoising,” *IEEE Transactions on Circuits and Systems for Video Technology*, 2024.
- [57] X. Lin, Y. Li, J. Hsiao, C. Ho, and Y. Kong, “Catch missing details: Image reconstruction with frequency augmented variational autoencoder,” in *Proceedings of the IEEE/CVF Conference on Computer Vision and Pattern Recognition*, 2023, pp. 1736–1745.
- [58] H. Sun, “Ultra-high resolution segmentation via boundary-enhanced patch-merging transformer,” 2024. [Online]. Available: <https://arxiv.org/abs/2412.10181>
- [59] S. Cheng and H. Sun, “Spt: Sequence prompt transformer for interactive image segmentation,” 2024. [Online]. Available: <https://arxiv.org/abs/2412.10224>
- [60] W. Ge, X. Lin, and Y. Yu, “Weakly supervised complementary parts models for fine-grained image classification from the bottom up,” in *Proceedings of the IEEE/CVF Conference on Computer Vision and Pattern Recognition*, 2019, pp. 3034–3043.
- [61] T. Ojala, M. Pietikainen, and T. Maenpaa, “Multiresolution gray-scale and rotation invariant texture classification with local binary patterns,” *IEEE Transactions on pattern analysis and machine intelligence*, vol. 24, no. 7, pp. 971–987, 2002.
- [62] D. G. Lowe, “Object recognition from local scale-invariant features,” in *Proceedings of the seventh IEEE international conference on computer vision*, vol. 2. Ieee, 1999, pp. 1150–1157.
- [63] G. Bouchard and B. Triggs, “Hierarchical part-based visual object categorization,” in *2005 IEEE Computer Society Conference on Computer Vision and Pattern Recognition (CVPR’05)*, vol. 1. IEEE, 2005, pp. 710–715.
- [64] H. Zhao, M. Tian, S. Sun, J. Shao, J. Yan, S. Yi, X. Wang, and X. Tang, “Spindle net: Person re-identification with human body region guided feature decomposition and fusion,” in *Proceedings of the IEEE conference on computer vision and pattern recognition*, 2017, pp. 1077–1085.
- [65] J. Xu, R. Zhao, F. Zhu, H. Wang, and W. Ouyang, “Attention-aware compositional network for person re-identification,” in *Proceedings of the IEEE conference on computer vision and pattern recognition*, 2018, pp. 2119–2128.
- [66] Z. Zhong, L. Zheng, Z. Luo, S. Li, and Y. Yang, “Invariance matters: Exemplar memory for domain adaptive person re-identification,” in *Proceedings of the IEEE/CVF conference on computer vision and pattern recognition*, 2019, pp. 598–607.
- [67] J. Song, Y. Yang, Y.-Z. Song, T. Xiang, and T. M. Hospedales, “Generalizable person re-identification by domain-invariant mapping network,” in *Proceedings of the IEEE/CVF conference on Computer Vision and Pattern Recognition*, 2019, pp. 719–728.
- [68] Y. Sun, L. Zheng, Y. Yang, Q. Tian, and S. Wang, “Beyond part models: Person retrieval with refined part pooling (and a strong convolutional baseline),” in *Proceedings of the European conference on computer vision (ECCV)*, 2018, pp. 480–496.
- [69] D. Li, X. Chen, Z. Zhang, and K. Huang, “Learning deep context-aware features over body and latent parts for person re-identification,” in *Proceedings of the IEEE conference on computer vision and pattern recognition*, 2017, pp. 384–393.
- [70] H. Yao, S. Zhang, R. Hong, Y. Zhang, C. Xu, and Q. Tian, “Deep representation learning with part loss for person re-identification,” *IEEE Transactions on Image Processing*, vol. 28, no. 6, pp. 2860–2871, 2019.
- [71] A. Dosovitskiy, L. Beyer, A. Kolesnikov, D. Weissenborn, X. Zhai, T. Unterthiner, M. Dehghani, M. Minderer, G. Heigold, S. Gelly *et al.*, “An image is worth 16x16 words: Transformers for image recognition at scale,” in *International Conference on Learning Representations*, 2020.
- [72] K. He, X. Zhang, S. Ren, and J. Sun, “Deep residual learning for image recognition,” in *Proceedings of the IEEE conference on computer vision and pattern recognition*, 2016, pp. 770–778.
- [73] Z. Lu, T. Pu, T. Chen, and L. Lin, “Content-aware hierarchical representation selection for cross-view geo-localization,” in *Proceedings of the Asian Conference on Computer Vision*, 2022, pp. 4211–4224.
- [74] T. Wang, Z. Zheng, Z. Zhu, Y. Sun, C. Yan, and Y. Yang, “Learning cross-view geo-localization embeddings via dynamic weighted decorrelation regularization,” *IEEE Transactions on Geoscience and Remote Sensing*, vol. 62, pp. 1–12, 2024.